



Systematic behavior of fragments in Bayesian neural network models for projectile fragmentation reactions

Chun-Wang Ma *, Xi-Xi Chen, Xiao-Bao Wei , Dan Peng, Hui-Ling Wei, Yu-Ting Wang, Jie Pu, Kai-Xuan Cheng, Ya-Fei Guo, and Chun-Yuan Qiao

College of Physics, Henan Normal University, Xinxiang 453007, China



(Received 14 May 2023; accepted 22 September 2023; published 11 October 2023)

The recently proposed Bayesian neural network (BNN) model was adopted to investigate the systematic behaviors of fragments cross sections produced in projectile fragmentation reactions. Mainly two phenomena are studied, i.e., (1) The scaling behavior in the difference between mass excess of mirror nuclei based on the binding energies of proton-rich fragments determined using the BNN-predicted cross sections for the $345A$ MeV $^{78}\text{Kr} + ^9\text{Be}$ reaction, which shows that the scaling phenomenon exists up to neutron excess $|I| = |N - Z|$ of 5; (2) the isobaric yield ratio distributions for mirror fragments [IYR(m)] produced in a series of projectile fragmentation reactions with projectiles of isotopes, isobars, and those that have the same neutron-skin thickness at different levels. The IYR(m) distributions predicted by the BNN model reflect the systematic evolution with neutron-skin thickness of projectile nuclei.

DOI: [10.1103/PhysRevC.108.044606](https://doi.org/10.1103/PhysRevC.108.044606)

I. INTRODUCTION

Fragments produced in projectile fragmentation reactions and their distributions are usually used to investigate the properties of reaction systems, as well as the properties of fragments themselves. Modern rare isotope facilities extend the primary nuclear beams from stable nuclei to rare isotopes, and attract much attention since they make it possible to discover new isotopes at neutron or proton drip lines [1]. For example, the Factory for Rare Isotope Beams (FRIB) at Michigan State University, USA, and the Radioactive Ion Beam Facility (RIBF) at RIKEN, Japan, show their strong ability to create new isotopes near/beyond drip lines. The recently discovered neutron-drip-line isotope ^{39}Na and neighboring nuclides at RIBF [2] and those closely distributed isotopes near the $N = 28$ main shell [3] called for high precision models for rare isotopes productions in projectile fragmentation reactions. Meanwhile, the precise predictions for fragments productions in projectile fragmentation reactions provide theoretical tools to systematically investigate reaction phenomena such as isospin effects in isotopic or mass distributions [4–6], fragment scaling phenomena [7], neutron-skin effects [8–10], as well as symmetric properties in mirror nuclei [11–13]. In particular, the isobaric yield ratios of fragments in projectile fragmentation reactions provide a clear probe to the chemical potential of protons and neutrons in reaction systems at the equilibrium stage of chemical freeze-out [14–17].

Among many models to predict fragments in projectile fragmentation reactions (see a review in Ref. [1]), such as transport models, empirical methods, parametrization formulas, and machine learning models, show significant

improvement in precision [18]. The newly proposed massive learning model based on Bayesian neural networks (BNNs) [18] provides the opportunity to systematically study the fragments' production and their evolving behavior in projectile fragmentation reactions induced by unstable nuclei, which motivated us to perform the work. In this article, using the BNN model, the scaling phenomenon in the difference between mass excess of mirror fragments and the isobaric yield ratio of mirror fragments [IYR(m)] in a series of projectile fragmentation reactions are explored. The parts of the article are the following: In Sec. II the adopted probes are introduced. In Sec. III the results are discussed. And in Sec. IV the work is summarized.

II. METHODOLOGIES

The main characteristics of the BNN model are introduced in Sec. II A, following which the correlation between isotopic cross section and its binding energy is introduced in Sec. II B, the symmetry in mass difference between mirror nuclei is described in Sec. II C, and the IYR(m) probe of neutron-skin thickness of asymmetric projectiles is introduced in Sec. II D.

A. BNN model

The BNN model proposed in Ref. [18] was constructed based on massive learning of 6393 fragments measured in 53 reactions, which aims at providing high-quality prediction of cross sections for fragments in projectile fragmentation reactions within a wide range of beam energy (from 40A MeV to 1A GeV), projectile mass (from $A = 40$ to 208), and projectile charge numbers (from $Z = 18$ to 82), as well as a wide range of fragments (from $Z = 3$ to those of the projectile nucleus). Systematic performance for reactions of typical projectile

*machunwang@126.com

beams at FRIB and RIBF facilities for the BNN model can be found in [19], which have been compared to predictions by EPAX3 and FRACS parametrizations. Typically, the BNN model predicted a 0.46 fb of ^{39}Na compared to an experimental estimation of 0.5 fb [19]. In this work, the BNN model was adopted to predict the projectile fragmentation reaction of 345A MeV $^{78}\text{Kr} + ^9\text{Be}$ to study the mirror nuclei symmetry, and a series of 140A MeV projectile fragmentation reactions to study the neutron-skin effects in the IYR(m) distribution. The readers are referred to Ref. [18] for detailed information about the BNN model.

B. Empirical correlation between binding energy and cross section

The method of using the isotopic cross section distribution to determine binding energy of a new isotope is traced to Ref. [20], in which an empirical formula between the cross section and average binding energy of a fragment is deduced in the canonical ensemble theory:

$$\sigma = C \exp[(\langle B' \rangle - 8)/\tau], \quad (1)$$

where $\langle B' \rangle = (B - \varepsilon_p)/A$ is the average binding energy of the fragment, and $\varepsilon_p = 1/2[(-1)^N + (-1)^Z]\varepsilon A^{-3/4}$ is the pairing energy ($\varepsilon = 30$ MeV). C and τ are free parameters, which can be determined from the $\sigma \sim \langle B' \rangle$ correlation. The correlation has been verified to be suitable both for fragments near the neutron drip line and those near the proton drip line [12,18,21,22]. In this article, the cross sections of proton-rich fragments are predicted by the BNN model, based on which the binding energies are determined and further studied in the mirror nuclei scaling phenomenon.

C. Mirror nuclei symmetry

A scaling phenomenon in mirror nuclei—i.e., the difference between their mass excess is linearly correlated to their residual Coulomb energies—has been observed, and it indicates the symmetric property in them. The scaling phenomenon can be described by the formula [11]

$$\begin{aligned} M(N - |I|, Z) - M(N, Z - |I|) \\ &= B(N, Z - |I|) - B(N - |I|, Z) - |I|(M_n - M_p) \\ &= a_c \delta_{\text{coul}} + a_{\text{sh}} \delta_{\text{sh}} - |I|(M_n - M_p), \end{aligned} \quad (2)$$

in which $a_{\text{sh}} \delta_{\text{sh}}$ is the shell correction to the separation energy of near-shell-closure nucleus, and M_n (M_p) is the mass of a free proton (neutron). a_c is the Coulomb-energy coefficient, and $\delta_{\text{coul}} = |I|A - |I|^2/3$. Based on the binding energies of fragments with $I = -4$ and -5 , which are determined from the $\sigma \sim \langle B' \rangle$ correlations predicted by the BNN model, the scaling phenomenon in the difference between mass excess of mirror nuclei is studied.

D. Isobaric yield ratio probe

In projectile fragmentation reactions, the cross section of a fragment is correlated to its free energy at the equilibrium stage. For example, in the modified Fisher model, the cross

section of a fragment (N, Z) is described as [23–25]

$$\begin{aligned} Y(I, A) = C_0 A^{-\tau} \exp\{[W(I, A) \\ + N\mu_n + Z\mu_p]/T\} + N \ln(N/A) + Z \ln(Z/A), \end{aligned} \quad (3)$$

where C_0 is a constant. $A^{-\tau}$ is related to the entropy of the residual fragment and τ is fixed for a specific reaction system but is varied with it. μ_n (μ_p) refers to the neutron (proton) chemical potential, which is related to the neutron density. The last two terms in the equation denote entropy contributions for the mixing of two substances. $W(I, A)$ is the free energy of fragment at temperature T , which could be described by the Weizsäcker-Bethe formula [26],

$$\begin{aligned} W(I, A) = -a_{\text{sym}} I^2/A - \delta(N, Z) \\ - a_c Z(Z - 1)/A^{1/3} + a_v A - a_s A^{2/3}, \end{aligned} \quad (4)$$

where the subindices of coefficients $i = v, s, \text{sym},$ and c denote the volume, surface, symmetry, and Coulomb- energies, respectively. All a_i are in forms of density- and temperature-dependent shape in the droplet model $a_i(\rho, T)$. $\delta(N, Z)$ is the pairing energy described as $\delta(N, Z) = (\text{sgn})a_p/A^{1/2}$, i.e., for the odd-odd and even-even fragment $\text{sgn} = 1$ and -1 , respectively. $\delta(N, Z) = 0$ for odd- A fragments.

Assuming that the nuclear density and temperature are the same for all fragments when they are formed, the IYR(m) for fragments with $|I| = 1$ is defined as [8,27,28],

$$\text{IYR(m)} = \ln(Y_{I=1}/Y_{I=-1}) = (\Delta\mu + a_c x)/T, \quad (5)$$

in which $a_c x$ has a form of residual Coulomb energy between the mirror nuclei, and $x \equiv 2(z - 1)/A^{1/3}$ (z refers to a fragment with $I = -1$). The deduction of this formula can be found in Refs. [8,25]. $\Delta\mu \equiv \mu_n - \mu_p$ denotes the difference between chemical potentials of neutrons and protons, which also indicates the density variation in different reaction systems and provides a tool to indicate the change of neutron-skin thickness (δ_{np}) of asymmetric projectile nuclei. The δ_{np} of an asymmetric nucleus is defined as the difference between its root-mean-square (rms) radii of neutrons and protons distributions,

$$\delta_{np} = \sqrt{\langle r_n^2 \rangle} - \sqrt{\langle r_p^2 \rangle}, \quad (6)$$

The Fermi-type density distributions for neutrons and protons are adopted to determine the neutron skin thickness of nuclei,

$$\rho_i(r) = \frac{\rho_i^0}{1 + \exp\left(\frac{r - C_i^{1/2}}{t_i/4.4}\right)}, \quad i = n, p, \quad (7)$$

where $i = n, p$ denotes neutrons and protons, respectively. ρ^0 is a normalization constant. t_i is the diffuseness parameter, and is calculated by

$$t_i = 4.55/\sqrt{(A - Z)s_i}, \quad (8)$$

in which s_i is the separation energy of the valence neutron or proton.

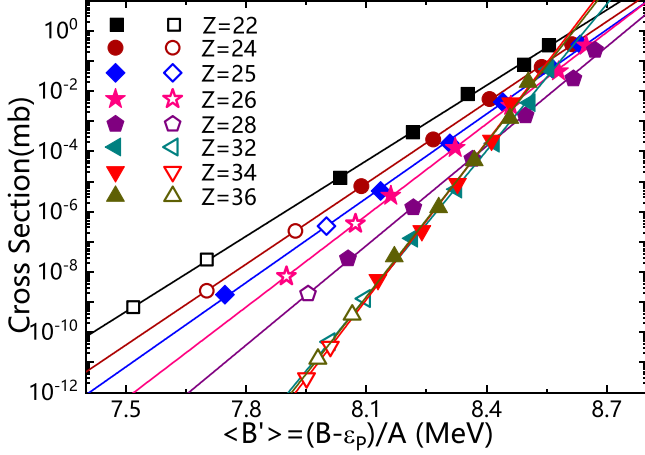


FIG. 1. The correlation between the isotopic cross section and its $\langle B' \rangle$ for fragments produced in the 345A MeV $^{78}\text{Kr} + ^9\text{Be}$ reaction (measured data taken from [30]). The full (open) symbols denote the BNN-predicted (measured) cross sections for fragments. The lines denote linear fitting results to the correlation for BNN-predicted fragments.

$C^{1/2}$ is the radius at the half-density distribution. In the droplet model is calculated by

$$C_i = R_i[1 - (b_i/R_i)^2], \quad (9)$$

in which $b_i = 0.413t_i$ [29].

The rms radius for the neutron (proton) distribution is calculated by

$$\sqrt{\langle r_i^2 \rangle} = \left[\frac{\int r^2 \rho_{n(p)}(r) d\tau}{\int \rho_{n(p)}(r) d\tau} \right]^{1/2}, \quad (10)$$

in which the nuclear density distribution is described by Eq. (7).

III. RESULTS AND DISCUSSION

A. Scaling of mirror nuclei mass difference

According to Eq. (1), the binding energies of proton-rich isotopes for Z from 22 to 36 are deduced from their BNN predicted cross sections in the 345A MeV $^{78}\text{Kr} + ^9\text{Be}$ reaction. Both measured proton-rich isotopes (open symbols) and BNN predicted ones (full symbols) are plotted in Fig. 1. The BNN-predicted fragments are from $I = -3$ to 1, and the measured proton-rich ones are for $I = -4$ and $I = -5$. The correlations between the BNN-predicted isotopic cross section distributions and $\langle B' \rangle$ are used to determine C and τ for each isotopic chain by performing a linear fitting analysis (denoted by lines), following which $\langle B' \rangle$ and B for the measured fragments with $I = -4$ and $I = -5$ are determined (labeled as $\langle B' \rangle_{\text{BNN}}$ and B_{BNN}). Compared to the data in AME2020 [31], the binding energies determined from isotopic cross section distributions (see Table I) have relatively small differences, with $\delta B \equiv \frac{B_{\text{BNN}} - B_{\text{AME}}}{B_{\text{AME}}} \%$ smaller than $\pm 1.5\%$ except for ^{40}Ti and ^{67}Kr , indicating that the parameters C and τ for each isotopic chain are reasonable.

TABLE I. Binding energies for proton-rich nuclides determined from isotopic cross section distributions in the 345A MeV $^{78}\text{Kr} + ^9\text{Be}$ reaction [30]. $\langle B_{\text{BNN}} \rangle$ denotes the average binding energies from BNN-predicted cross sections. $\langle B_{\text{AME}} \rangle$ denote the binding energies in AME2020 [31] (values with and without asterisks denote the measured and evaluated results, respectively). The quantity δB is defined as $\delta B \equiv \frac{B_{\text{BNN}} - B_{\text{AME}}}{B_{\text{AME}}} \%$.

$^A Z$	I	$\langle B' \rangle_{\text{BNN}}$	$\langle B' \rangle_{\text{AME}}$	B_{BNN}	B_{AME}	δB
^{39}Ti	-5	7.5175	7.566	293.1825	295.0740	-0.6410
^{40}Ti	-4	7.7072	7.8656*	308.2880	314.6240	-2.0138
^{43}Cr	-5	7.7013	7.6800	331.1559	330.2400	0.2773
^{44}Cr	-4	7.9230	7.9496*	348.6120	349.7824	-0.3346
^{46}Mn	-4	8.0004	7.9161*	368.0184	364.1406	1.0649
^{47}Fe	-5	7.9004	7.7900	371.3188	366.1300	1.4172
^{48}Fe	-4	8.0727	8.0227*	387.4896	385.0896	0.6232
^{51}Ni	-5	7.9547	7.8700	405.6897	401.3700	1.0762
^{59}Ge	-5	8.0086	7.9240	472.5074	467.5160	1.0676
^{60}Ge	-4	8.0707	8.1130	484.2420	486.7800	-0.5214
^{63}Se	-5	7.9867	7.9170	503.1621	498.7710	0.8804
^{64}Se	-4	8.0647	8.0750	516.1408	516.8000	-0.1276
^{67}Kr	-5	7.7399	7.8830	518.5733	528.1610	-1.8153
^{68}Kr	-4	7.9990	8.0340	543.9320	546.3120	-0.4356

The scaling phenomenon in the difference between mass excess of mirror nuclei is plotted in Fig. 2 for fragments with $|I|$ from 1 to 5. The fragments studied in this work are near magic numbers of 20 and 28, which are sensitive to the shell evolution. In Eq. (2), the shell corrections must be considered.

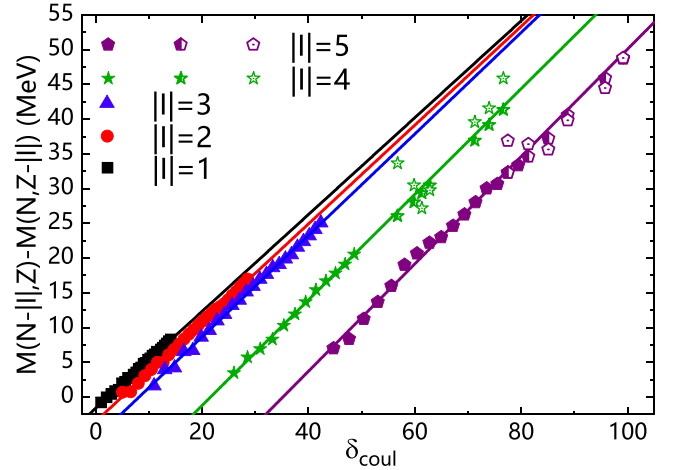


FIG. 2. The scaling of mass difference and residual Coulomb energy between mirror nuclei with $|I| = 1$ to 5. The y axis is the difference $M(N - |I|, Z) - M(N, Z - |I|)$ between mirror nuclei with $|I|$. The x axis is the residue Coulomb energy between mirror nuclei according to Eq. (2). The full symbols denote results from AME2020 [31]. The open symbols denote those predicted from isotopic cross sections by BNN model in the 345A MeV $^{78}\text{Kr} + ^9\text{Be}$ reaction as listed in Table I. The half-full symbols also denote the results from AME2020 but for a clearer comparison to BNN predictions. For clarity, δ_{coul} for $|I| = 4$ and 5 mirror nuclei are shifted by +10 and +20, respectively.

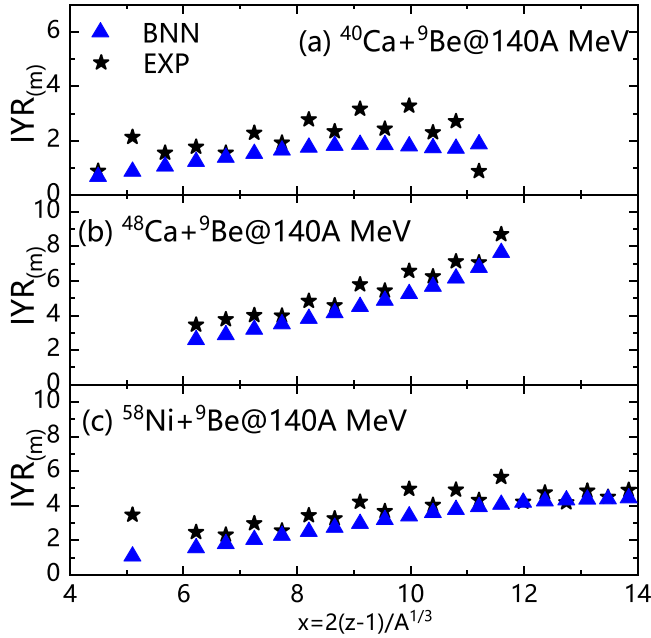


FIG. 3. The IYR(m) distributions for the 140A MeV $^{40}\text{Ca} + ^9\text{Be}$ (a), $^{48}\text{Ca} + ^9\text{Be}$ (b) and $^{58}\text{Ni} + ^9\text{Be}$ (c) projectile fragmentation reactions. The predicted IYR(m) distributions by BNN are plotted as triangles. The experimental IYR(m) distributions (stars) are based on results in Ref. ([32]).

According to Ref. [11], δ_{sh} equals 1, 2, 3, 4, 5, or 6 for proton number Z (or neutron number N) in the ranges 1–2, 3–8, 9–20, 21–28, 29–50, and 51–82. $a_{\text{sh}} = -0.142, -0.3, -0.35, \text{ and } -0.425$ MeV are taken for $|I|$ from 1 to 4 [11]. For the measured binding energy of mirror nuclei (full and half full symbols) in AME2020 [31], the scaling law according to Eq. (2) is well obeyed, in which the difference in mass excess between mirror nuclei shows a strong linear correlation to their residual Coulomb energy. Compared to the corresponding $|I| = 4$ and 5 mirror nuclei in AME2020 (half-full symbols), the mass differences based on the deduced results in Table I (open symbols) are shown. For the $|I| = 4$ mirror nuclei, the predicted mass difference by the BNN model obeys Eq. (2) well except for a few of them. Since no value of a_{sh} for $|I| = 5$ was recommended, with $a_{\text{sh}} = 0.9$ MeV the predicted mass difference by the BNN model reproduces well the scaling phenomenon for them.

B. Neutron-skin effects in IYR(m)

In this section, the influence of neutron-skin thickness on IYR(m) is discussed. First, we discuss the results in projectile fragmentation reactions of 140A MeV ^{40}Ca , ^{48}Ca , ^{58}Ni bombarding a ^9Be target, of which the fragments were measured by Mocko *et al.* [32]. The BNN predicted IYR(m) distributions are compared to the measured ones in Fig. 3. For the ^{48}Ca and ^{58}Ni reactions, the BNN predictions agree with the experiments. In general, the IYR(m) distribution depends on x linearly for both the experimental and BNN predictions for fragments of relatively small x . For fragments of larger x , IYR(m) tends to decrease with the increasing x

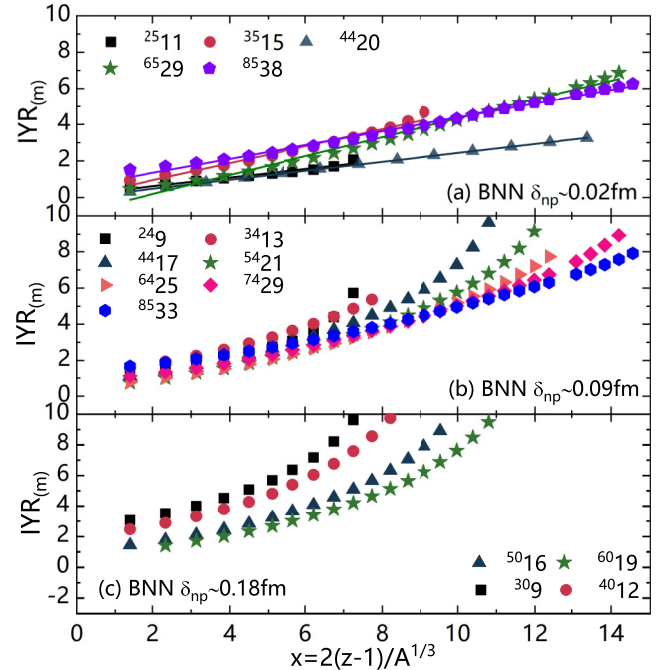


FIG. 4. The IYR(m) distributions for 140A MeV $^AZ + ^9\text{Be}$ reactions predicted by the BNN model. Panels (a), (b), and (c) are for projectile nuclei with $\delta_{np} \approx 0.02, 0.09, \text{ and } 0.18$ fm, respectively. The lines in panel (a) denote the linear fitting to the IYR(m) and x correlations.

for reactions of the symmetric projectile (^{40}Ca) and increases with x for a neutron-rich projectile (^{48}Ca). The dependence of IYR(m) on x indicates that the fragments are sensitive to the neutron-skin structure of projectile nuclei, as discussed in Refs. [8,33].

The IYR(m) distribution shows a strong dependence on δ_{np} of the projectile nucleus [14–16]. Second, we predict IYR(m) distributions in reactions of projectile nuclei with similar δ_{np} , which are $\delta_{np} \approx 0.02, 0.09, \text{ and } 0.18$ fm determined by Fermi-type distributions. For $\delta_{np} \approx 0.02$ fm, which have similar proton and neutron density distributions, the selected projectiles are $^{25}\text{11}, ^{35}\text{15}, ^{44}\text{20}, ^{65}\text{29}, \text{ and } ^{85}\text{38}$. For $\delta_{np} \approx 0.09$ fm, the projectiles are $^{24}\text{9}, ^{34}\text{13}, ^{44}\text{17}, ^{54}\text{21}, ^{64}\text{25}, ^{74}\text{29}, \text{ and } ^{85}\text{33}$. For $\delta_{np} \approx 0.18$ fm, the projectiles are $^{30}\text{9}, ^{40}\text{12}, ^{50}\text{16}, \text{ and } ^{60}\text{19}$. In Fig. 4, the BNN predicted IYR(m) distributions are plotted. For projectiles with $\delta_{np} \approx 0.02$ fm, the IYR(m) distributions show good linear correlation to x as seen in Fig. 4(a). For projectiles with $\delta_{np} \approx 0.09$ fm, the IYR(m) distribution shows linear correlation with x for fragments with small x , and then IYR(m) are enhanced and deviate from linear correlation for fragments with large x . For projectiles with $\delta_{np} \approx 0.18$ fm, the linear part of IYR(m) generally disappears and IYR(m) increases with x much quicker.

The linear IYR(m) $\sim x$ correlation for mirror nuclei in Eq. (5) is well reproduced in Fig. 4(a) for projectiles without neutron skin, but the deviations from linear correlation are also observed in Figs. 4(b) and 4(c) for projectiles with neutron skin. The slope of the IYR(m) $\sim x$ correlation reflects a_c/T in Eq. (5), indicating that a_c/T is not only definitely

influenced by the temperature when the fragments are formed, but also depends on the nuclear density in the reaction. We tried to explain the deviation of $IYR(m) \sim x$ from both sides of nuclear density and temperature of the reaction. To do this, one assumes the projectile nucleus has a “core” and a “surface” according to the Fermi-type density distribution. In the core, the protons have a uniform density distribution, and so do the neutrons. In the surface region, both the neutron- and proton-density distributions decrease fast with the increasing radius. For a neutron-rich projectile, the density of neutrons decreases slower than that of protons. One also assumes that the central collisions are induced by the core of the projectile, while the peripheral collisions are induced by the surface of the projectile. One then has the following results.

- (1) The linear $IYR(m) \sim x$ correlation is well obeyed in the whole range of mirror fragments in Fig. 4(a) for projectiles without neutron skin, in which the proton and neutron density distributions are very similar. This indicates that the slope (a_c/T) extracted from the correlation depends on the uniformity of proton and neutron distributions.
- (2) The increased distortion of linear $IYR(m) \sim x$ correlation in Fig. 4(b) could be assumed to be influenced by the enlarged difference between neutron-density and proton-density distributions. The enhanced distortion of $IYR(m) \sim x$ correlation from the linear one in fragments with large mass could be accounted for by the enlarged difference between neutron-density and proton-density distributions in the surface (peripheral) region (collisions), i.e., the neutron-skin effect.
- (3) The explanation of the $IYR(m) \sim x$ distributions in Fig. 4(b) could also explain the phenomenon in Fig. 4(c).
- (4) Items (1) to (3) indicate the conclusion that the distortion of the linear $IYR(m) \sim x$ correlation reflects the uniformity of neutron- and proton-density distributions.
- (5) The temperature difference between central collisions and peripheral collisions is only shown in light-mass fragments. Based on the results of isotopic thermometers, the temperatures of intermediate-mass and large-mass fragments are very similar (most of them are around $T \approx 1$ MeV) [34].

It is likely that the deviation of $IYR(m) \sim x$ from linear correlation is because of the neutron-skin structures of neutron-rich projectiles.

Before the discussion on the systematic behavior of $IYR(m)$ in reactions, a quantity $\Delta IYR(m)$ is defined to denote the $IYR(m)$ difference between asymmetric and symmetric systems. The symmetric reaction is also considered the reference system, of which the projectile nucleus has $\delta_{np} \approx 0$. According to Eq. (5), $\Delta IYR(m)$ has the form

$$\Delta IYR(m) \equiv IYR(m)_{\text{asy}} - IYR(m)_{\text{sym}} = \Delta\mu_{21}/T, \quad (11)$$

in which $IYR(m)_{\text{asy}}$ and $IYR(m)_{\text{sym}}$ denote the $IYR(m)$ for asymmetric and symmetric reactions. $\Delta\mu_{21}/T$ quantifies the difference between $\Delta\mu/T$ of two reactions. $\Delta\mu$ indicates the difference between the chemical potentials of a neutron and

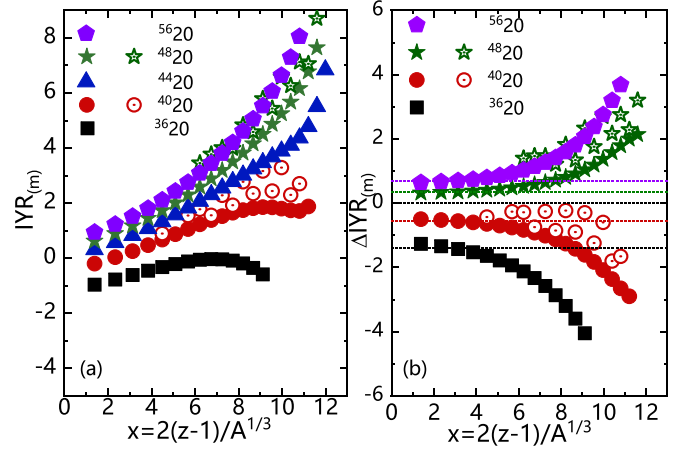


FIG. 5. (a): The $IYR(m)$ distributions for 140A MeV $^{36,40,44,48,56}\text{Ca} + ^9\text{Be}$ reactions predicted by the BNN model (solid symbols), and compared to measured ones (open symbols) for $^{40,48}\text{Ca} + ^9\text{Be}$ reactions. (b) $\Delta IYR(m)$ for two reactions with $IYR(m)$ of the ^{44}Ca reaction as the reference.

proton in one reaction system, which reflects the degree of uniformity for neutron and proton distribution. $\Delta\mu_{21}$ thus reflects the difference of neutron and proton density distributions between the asymmetric reaction and the reference one.

Third, we investigate the evolution of $IYR(m)$ distributions in reactions induced by isotopic projectiles for 140A MeV $^{36,40,44,48,56}\text{Ca} + ^9\text{Be}$. From ^{36}Ca to ^{56}Ca , δ_{np} of projectile nuclei are -0.117 , -0.05 , 0.005 , 0.053 , and 0.129 fm, respectively. For ^{44}Ca , $\delta_{np} \approx 0$, which indicates that isotopes smaller than it have proton-skin structures and those larger than it have neutron-skin structures. For the BNN predictions, as shown in Fig. 5(a), the $IYR(m)$ distributions increase as the projectile nucleus becomes more neutron rich. Similar trends of $IYR(m)$ in the reactions can be found in Fig. 3, i.e., the $IYR(m)$ has the structure of a “linear part” plus a “nonlinear (decreasing or increasing)” part with x . As the linear correlation $IYR(m) \sim x$ reflects the uniform density distributions of neutrons and protons, the nonlinear parts of the $IYR(m)$ distribution indicate the neutron- and proton-skin structures. The $IYR(m)$ distributions decrease clearly for large fragments with increasing x in reactions induced by ^{36}Ca and ^{40}Ca , while they increase more quickly in reactions induced by ^{48}Ca and ^{56}Ca . In Fig. 5(b), the $\Delta IYR(m)$ are plotted by selecting $^{44}\text{Ca} + ^9\text{Be}$ as the reference reaction. The $\Delta IYR(m)$ distribution can be viewed, not very strictly, as being composed of a plateau plus the accelerated dropping part for $^{36,40}\text{Ca} + ^9\text{Be}$ reactions or the accelerated increasing part for $^{48,56}\text{Ca} + ^9\text{Be}$ reactions. One also considers the “core + surface” structure of a nucleus in the Fermi-type density distribution. The plateau indicates the difference between the neutron and proton density distributions in the core of projectile nuclei, while the accelerated part in $\Delta IYR(m)$ reflects the enlarged difference between neutron and proton density distributions of two projectile nuclei in the surface regions. If one assumes that the proton nuclear density distributions of calcium isotopes are very similar, $\Delta IYR(m)$ reflects the difference between the asymmetric projectile and the reference (^{44}Ca).

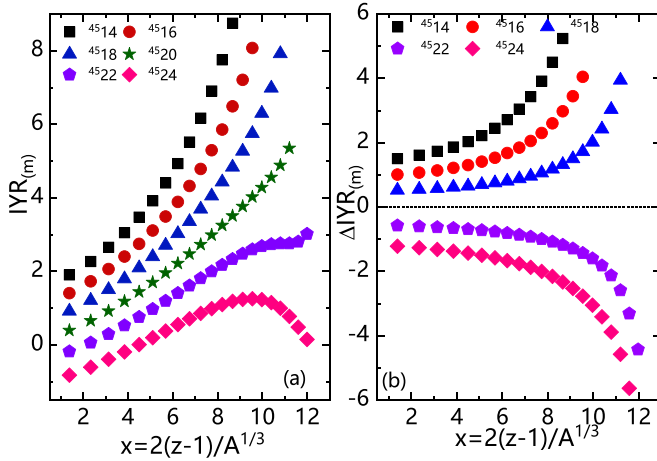


FIG. 6. (a) The IYR(m) distributions for 140A MeV $^{45}\text{Z} + ^9\text{Be}$ reactions predicted by the BNN model. Z of the isobaric projectile nucleus ranges from 14 to 24. (b) $\Delta\text{IYR}(m)$ for two reactions with IYR(m) of the ^{45}Ca reaction as the reference one.

Finally, we further investigate the IYR(m) distributions in reactions of $A = 45$ isobaric projectile nuclei, i.e., 140A MeV $^{45}\text{Z} + ^9\text{Be}$. The selected projectile nuclei, beginning from the neutron-rich value of $Z = 14$ to the proton-rich value $Z = 24$ in steps of $Z = 2$, have $\delta_{np} = 0.179, 0.127, 0.073, 0.018, -0.038,$ and -0.096 fm, respectively. For isobaric projectiles, it can be assumed to have no volume effect induced by the reaction system, with the result that IYR(m) simply depends on the neutron-skin thickness of the projectile nucleus. In Fig. 6(a), as the projectile nucleus is changed from the proton-rich one to the neutron-rich one, IYR(m) distributions are found that are similar to those in calcium isotopic projectiles, i.e., the proton-skin structure makes the IYR(m) distribute drop from the linear correlation for larger mass fragments and the neutron-skin structure makes it increase quicker from the linear correlation. For the projectile nucleus of $\delta \approx 0$, IYR(m) generally shows good linear correlation to x for a wide range of fragments. The reaction of $^{45}\text{Z} + ^9\text{Be}$ is selected as the reference system, and $\Delta\text{IYR}(m)$ are calculated for asymmetric reaction systems. In Fig. 6(b), $\Delta\text{IYR}(m)$ for the $A = 45$ isobaric projectile fragmentation reactions are plotted, and show the clear influence of IYR(m) by the neutron-skin thickness.

Based on the above discussion, the IYR(m) distribution in reactions induced by projectile nuclei without neutron-skin thickness is found to be linearly correlated to x of fragments. The deviation of IYR(m) from linear correlation, in reactions

induced by projectiles with both proton and neutron skin, is sensitive to the skin thickness. Based on the $\Delta\text{IYR}(m)$ distributions of mirror fragments between asymmetric and symmetric projectile fragmentation reactions, we propose using it as a probe for nuclear density distribution in the asymmetric projectile nuclei by referring to the IYR(m) distribution for which the projectile has the same neutron and proton density distributions.

IV. SUMMARY

In summary, the recently proposed BNN model for projectile fragmentation reactions is adopted to investigate the systematic behaviors of mirror nuclei. Two phenomena related to fragment production in projectile fragmentation reactions are studied, i.e., the scaling in difference of mass excess between mirror fragments, and the systematic evolution of IYR(m) in projectile fragmentation reactions.

In the first part, the cross sections of proton-rich isotopes in the 140A MeV $^{78}\text{Kr} + ^9\text{Be}$ reaction are predicted using the BNN model, and then they are further used to verify the scaling phenomenon of the mass difference between mirror nuclei. For mirror nuclei with $|I|$ from 1 to 4, the scaling in the difference between their mass excess can be observed in both the AME2020 and the BNN predicted binding energies. Meanwhile, with the selected coefficient of shell correction, the scaling phenomena can be well reproduced for mirror nuclei with $I = 5$.

The neutron-skin effects in IYR(m) distributions predicted by the BNN model are studied. Four types of reactions are calculated: (1) The 140A MeV $^{40}\text{Ca} / ^{48}\text{Ca} / ^{58}\text{Ni} + ^9\text{Be}$ reactions of which measured data exist; (2) the projectiles with same neutron-skin thickness at different levels; (3) the isotopic projectiles of 140A MeV $^{36,40,44,48,56}\text{Ca} + ^9\text{Be}$ reactions; and (4) the isobaric projectiles of 140A MeV $^{45}\text{Z} + ^9\text{Be}$ reactions. The BNN-predicted IYR(m) distributions reflect the systematic evolution phenomenon with the change of neutron skin in projectile nuclei. It is suggested that IYR(m) or $\Delta\text{IYR}(m)$ could serve as probes for neutron-skin thickness.

ACKNOWLEDGMENTS

This work is supported by the National Natural Science Foundation of China (Grant No. 11975091) and the Program for Innovative Research Team (in Science and Technology) of the University of Henan Province (Grant No. 21IRTSTHN011), China.

[1] C. W. Ma, H. L. Wei, X. Q. Liu *et al.*, *Prog. Part. Nucl. Phys.* **121**, 103911 (2021).
 [2] D. S. Ahn, J. Amano, H. Baba *et al.*, *Phys. Rev. Lett.* **129**, 212502 (2022).
 [3] H. L. Crawford, V. Tripathi, J. M. Allmond *et al.*, *Phys. Rev. Lett.* **129**, 212501 (2022).
 [4] C. W. Ma, H. L. Wei, J. Y. Wang *et al.*, *Phys. Rev. C* **79**, 034606 (2009).

[5] B. Li, N. Tang, Y. H. Zhang *et al.*, *Nucl. Sci. Tech.* **33**, 55 (2022).
 [6] L. Li, F. Y. Wang, and Y. X. Zhang, *Nucl. Sci. Tech.* **33**, 58 (2022).
 [7] C. W. Ma, Y. D. Song, C. Y. Qiao *et al.*, *J. Phys. G: Nucl. Part. Phys.* **43**, 045102 (2016).
 [8] C. W. Ma, H. L. Wei, and Y. G. Ma, *Phys. Rev. C* **88**, 044612 (2013).

- [9] H. L. Wei, X. Zhu, and C. Yuan, *Nucl. Sci. Tech.* **33**, 111 (2022).
- [10] C. W. Ma, Y. P. Liu, H. L. Wei *et al.*, *Nucl. Sci. Tech.* **33**, 6 (2022).
- [11] M. Bao, Y. Lu, Y. M. Zhao, and A. Arima, *Phys. Rev. C* **94**, 044323 (2016).
- [12] C. W. Ma, Y. D. Song, and H. L. Wei, *Sci. China Phys. Mech. Astron.* **62**, 012013 (2019).
- [13] Y. Y. Zong, C. Ma, M. Q. Lin, and Y. M. Zhao, *Phys. Rev. C* **105**, 034321 (2022).
- [14] C.-W. Ma, S. S. Wang, Y. L. Zhang, and H. L. Wei, *Phys. Rev. C* **87**, 034618 (2013).
- [15] C. W. Ma, J. Yu, X. M. Bai, Y. L. Zhang, H. L. Wei, and S. S. Wang, *Phys. Rev. C* **89**, 057602 (2014).
- [16] C. Y. Qiao, H. L. Wei, C. W. Ma, Y. L. Zhang, and S. S. Wang, *Phys. Rev. C* **92**, 014612 (2015).
- [17] C. W. Ma, H. L. Wei, S. S. Wang *et al.*, *Phys. Lett. B* **742**, 19 (2015).
- [18] C. W. Ma, X. B. Wei, X. X. Chen *et al.*, *Chin. Phys. C* **46**, 074104 (2022).
- [19] X. B. Wei, H. L. Wei, Y. T. Wang *et al.*, *Nucl. Sci. Tech.* **33**, 155 (2022).
- [20] M. B. Tsang, W. G. Lynch, W. A. Friedman, M. Mocko, Z. Y. Sun, N. Aoi, J. M. Cook, F. Delaunay, M. A. Famiano, H. Hui, N. Imai, H. Iwasaki, T. Motobayashi, M. Niikura, T. Onishi, A. M. Rogers, H. Sakurai, H. Suzuki, E. Takeshita, S. Takeuchi *et al.*, *Phys. Rev. C* **76**, 041302(R) (2007).
- [21] Y.-D. Song, H.-L. Wei, and C.-W. Ma, *Chin. Phys. C* **42**, 074102 (2018).
- [22] D. Peng, H. L. Wei, X. X. Chen *et al.*, *J. Phys. G: Nucl. Part. Phys.* **49**, 085102 (2022).
- [23] R. W. Minich, S. Agarwal, A. Bujak *et al.*, *Phys. Lett. B* **118**, 458 (1982).
- [24] A. S. Hirsch, A. Bujak, J. E. Finn *et al.*, *Nucl. Phys. A* **418**, 267 (1984).
- [25] C. W. Ma, F. Wang, Y. G. Ma, and C. Jin, *Phys. Rev. C* **83**, 064620 (2011).
- [26] C. F. von Weizsäcker, *Z. Phys.* **96**, 431 (1935).
- [27] S. R. Souza and M. B. Tsang, *Phys. Rev. C* **85**, 024603 (2012).
- [28] M. Huang, Z. Chen, S. Kowalski *et al.*, *Phys. Rev. C* **81**, 044620 (2010).
- [29] W. D. Myers and K.-H. Schmidt, *Nucl. Phys. A* **410**, 61 (1983).
- [30] B. Blank, T. Goigoux, P. Ascher *et al.*, *Phys. Rev. C* **93**, 061301 (2016).
- [31] M. Wang, W. J. Huang, F. G. Konder *et al.*, *Chin. Phys. C* **45**, 030003 (2021).
- [32] M. Mocko, M. B. Tsang, L. Andronenko, M. Andronenko, F. Delaunay, M. Famiano, T. Ginter, V. Henzl, D. Henzlova, H. Hua, S. Lukyanov, W. G. Lynch, A. M. Rogers, M. Steiner, A. Stolz, O. Tarasov, M. J. van Goethem, G. Verde, W. S. Wallace, and A. Zalessov, *Phys. Rev. C* **74**, 054612 (2006).
- [33] C. W. Ma, X. M. Bao, J. Yu *et al.*, *Eur. Phys. J. A* **50**, 139 (2014).
- [34] C.-W. Ma, S.-S. Wang, J. Pu *et al.*, *Commun. Theor. Phys.* **59**, 95 (2013).